Journal of Physics D: Applied Physics

PAPER • **OPEN ACCESS**

Optical and electrical optimization of all-perovskite pin type junction tandem solar cells

To cite this article: Marcos Soldera *et al* 2020 *J. Phys. D: Appl. Phys.* **53** 315104

OPEN ACCESS
IOP Publishing
Journal of Physics D: Applied Physics
J. Phys. D: Appl. Phys. **53** (2020) 315104 (13pp)
https://doi.org/10.1088/1361-6463/ab8851

Optical and electrical optimization of all-perovskite pin type junction tandem solar cells

Marcos Soldera[1,2], **Alejandro Koffman-Frischknecht**[1] **and Kurt Taretto**[1]

[1] Instituto de Investigación y Desarrollo en Ingeniería de Procesos, Biotecnología y Energías Alternativas (PROBIEN, CONICET-UNCo), 8300 Neuquén, Argentina
[2] Institut für Fertigungstechnik, Technische Universität Dresden, 01062 Dresden, Germany

E-mail: marcos.soldera@mailbox.tu-dresden.de

Received 24 October 2019, revised 5 February 2020
Accepted for publication 9 April 2020
Published 1 June 2020

Abstract

A definitive breakthrough of perovskite solar cells towards large scale industrialization is believed to be the demonstration of higher efficiencies than conventional silicon technology, suggesting the exploration of perovskite tandem cell configurations. Since high efficiency tandem solar cells require careful optimization of photoactive as well as contact and additional functional layers, we propose an optical-electrical model to obtain the optimum layer thicknesses and the attainable electrical output parameters of two-terminal perovskite-perovskite tandem solar cells. The optical model takes into account the coherent propagation of light through the layer stack comprising two perovskite semiconductors and the corresponding contact layers, while the electrical model assumes two series-connected analytical current/voltage equations for pin solar cells. This model allows to assess the impact of the main physical parameters on each perovskite layer without requiring the high specificity needed in more rigorous numerical simulations. Efficiencies above 34% are predicted considering available perovskites with non-optimum bandgap and contact materials already proven in efficient laboratory solar cells. The requisite to attain such efficiencies is that recombination at the interfaces between the perovskite and contact materials is kept low in both bottom and top cells. Furthermore, within the assumption of non-optimum bandgaps of currently available perovskites, the simulation results suggest that efficiencies around 37% are possible when adopting contact materials with smaller absorption, more adequate refraction indices, and lower resistivity.

Keywords: perovskite, tandem solar cells, electrical modelling, optical simulations, optimization

Supplementary material for this article is available online

(Some figures may appear in colour only in the online journal)

1. Introduction

In the last decade, organic-inorganic perovskite semiconductors have attracted the attention of the photovoltaics community due to their outstanding optoelectronic properties which boosted single (i.e. monojunction) solar cell efficiencies beyond 23% [1]. Some of the extraordinary features these materials offer are their relatively long electron and hole diffusion lengths exceeding 1 μm, absorption coefficients well above 10^4 cm^{-1}, high electronic defect tolerances and bandgap tunability, combined with the potential for low cost processing [2–6]. Envisioning that state of the art single junction perovskite solar cells are approaching their theoretical limit of

31% imposed by the Schockley–Queisser theory [7], new approaches based on third generation photovoltaics need to be conceived to surpass this limit. One of such concepts is the use of multijunction solar cells, where the bandgaps of two or more photoactive materials are engineered to absorb complementary portions of the solar spectrum, reducing thermalization losses [8]. The Shockley–Queisser theory shows that if silicon is used as the bottom absorber in two-junction tandem cell, the ideal bandgap of the top semiconductor lies around 1.5–1.6 eV, which matches the bandgap of high-performing perovskites, such as $CH_3NH_3PbI_3$ (MAPI, MA = methylammonium) [9], $HC(NH2)_2PbI_3$ (FAPI, FA = formamidinium) [10] and triple cation perovskites [11]. Using these materials, efficiencies around 25% [12] and 28% [1] have already been demonstrated in two-terminal tandem cells. However, these cells remain in the efficiency order of the best silicon single junction cells with a world record efficiency of 26.7% [13]. Besides, it is not yet clear if the lifetime of the perovskite sub-cell can even match the long lifetime of a typical silicon cell of more than 25 years. Despite all-perovskite tandem solar cells could also suffer from a short lifetime, their potential low processing costs make these devices an attractive alternative to conventional silicon based photovoltaics for niche markets. Recently, it was reported a mechanically stacked all-perovskite tandem cell with an impressive efficiency record of 25% [14], where the top absorber is the perovskite $Cs_{0.05}FA_{0.8}MA_{0.15}PbI_{2.55}Br_{0.45}$ with a bandgap of 1.63 eV and the bottom absorber is a guanidinium thiocyanate modified $(FASnI_3)_{0.6}(MAPbI_3)_{0.4}$ perovskite with a bandgap of 1.25 eV. Considering that the theoretical efficiency limit for these materials is 45% [15], there is still plenty of room for further optimization efforts.

In order to improve the efficiency of the state of the art all-perovskite tandem cells, the device structure comprising all the photoactive, contact and functional layers must be carefully designed. Considering that, currently, pin junctions are the most common device structure for perovskite tandem cells, the selection of appropriate contact layers determines the built-in voltage in each perovskite sub-cell, the internal electric field and, to a large extent, the cell's electric output parameters. The selection of functional layers defines also the interface recombination at the semiconductor/contact interfaces and the device series resistance, which can strongly affect the resulting device efficiency [16–18]. Moreover, optimization of the layer stack is not only dictated by electrical performance alone, since the maximum achievable sunlight absorbance depends strongly on the complex refractive index of the chosen perovskites and contact layers, as well as their thicknesses [19]. Therefore, the influence of such large amount of variables on the device performance can only be thoroughly analyzed using appropriate optical-electrical models.

In this contribution, we combine well-established models to predict the output parameters of two-terminal tandem cells based in perovskite absorbers and state of the art contact layers. The optical behavior is simulated employing the generalized transfer matrix method [20, 21], which accounts for interference effects in the thin film layer stack, as well as absorption within each layer and reflection at all interfaces. To optimize the stack, a simulated annealing optimization algorithm is used to maximize the resulting photocurrent with current matching conditions between both sub-cells. The calculated photocurrent is afterwards used as input in an analytical drift-diffusion electrical model [22], which provides the resulting power conversion efficiency and other electrical output parameters. The impact of perovskite carrier transport properties, namely carrier lifetime and mobility, as well as interface recombination velocity at the interfaces, internal built-in voltage and series resistance on the device behavior is investigated. Finally, design guidelines for selecting the contact layers' materials are drawn from the simulations, aiming at all-perovskite tandem cells with efficiencies approaching 37%.

This manuscript is organized as follows: section 2 proposes a model to compute light absorption and electrical transport in tandem solar cells based on perovskites. Section 3 presents the results, discussing the practical implications and suggesting general guidelines for designing high-efficiency all-perovskite tandem cells. Section 4 explores the feasibility of increasing the device efficiency by replacing contact layers based on the results presented in section 3. Finally, in section 5 we draw the main conclusions of the obtained simulation results.

2. Model features

In order to select the perovskite layers according to their bandgap energies, we refer to [15], where the maximum theoretical efficiencies of tandem solar cells are evaluated as a function of the top and bottom bandgaps $E_{g,top}$ and $E_{g,btm}$, respectively. According to [15], a tandem cell optimized for AM1.5G illumination requires bandgaps of 1.61 eV and 0.94 eV for the series-connected top and bottom cells, respectively. As stated above, there are many perovskite semiconductors that have a bandgap close to 1.61 eV, however the lowest bandgaps reported on perovskites are on the order of 1.2–1.3 eV [23–25]. Among the plethora of readily available perovskite materials, we adopt two compounds which approach the best to the maximum theoretical efficiency, namely $Cs_{0.08}FA_{0.02}PbI_{2.31}Br_{0.61}Cl_{0.08}$, with $E_{g,top} = 1.75$ eV [26], and $CH_3NH_3Sn_{0.85}Pb_{0.15}I_3$, with $E_{g,btm} = 1.17$ eV [27]. According to [15], with the chosen bandgaps the theoretical efficiency is close to the optimum of about 46%. These perovskite materials are utilized throughout this work in the optical and electrical calculations.

2.1. Optical model

Rigorous optical modelling allows to optimize the layer stack in order to find the maximum attainable photocurrent keeping the condition of current matching for series connected, or two-terminals, tandem solar cell. In this study, the generalized transfer matrix method [20, 28, 29] is used to calculate the steady state electric field profile of solar radiation within the layer stack, which in turn enables to calculate the absorption in each layer as well as the total reflectance and the resulting photocurrent. This model assumes that all materials are homogeneous, linear and isotropic, and all the interfaces are parallel

and perfectly flat. As previous works have already shown, it is feasible to achieve interfaces with roughness well below the wavelength of visible light in perovskite-perovskite tandem devices [30–32], which, in practical terms, can be regarded as optically flat interfaces.

The air domain and the glass substrate are optically thick and therefore light propagates incoherently through them, suppressing the superposition of waves and interference phenomena. It is also assumed that the substrate is non-absorbing. Since the rest of the layers have thicknesses in the order of the wavelength of the used standard AM1.5G spectrum, it is assumed that light propagates coherently and thus interference effects can play a major role. The position x and wavelength λ dependent absorbed electromagnetic power $Q(x,\lambda)$ in a layer with a complex refractive index $\tilde{n}(\lambda) = n(\lambda) + i\kappa(\lambda)$ is calculated from the resulting electric field profile $\boldsymbol{E}(x,\lambda)$ as

$$Q(x,\lambda) = \frac{1}{2} c\varepsilon_0 n(\lambda)\,\alpha(\lambda)\,|E(x,\lambda)|^2, \tag{1}$$

where ε_0 is the permittivity of free space, c is the speed of light and $\alpha(\lambda) = 4\pi\kappa(\lambda)/\lambda$ is the absorption coefficient. Note that Q represents the density of the dissipated electromagnetic power in units of power per volume, typically W m^{-3}. Then the photocarrier generation profile $G(x,\lambda)$ in each of the photoactive materials can be obtained directly from the absorbed electromagnetic power as:

$$G(x,\lambda) = Q(x,\lambda)\,/\,(hc/\lambda), \tag{2}$$

where h is Planck's constant. Finally, the maximum attainable photocurrent in each sub-cell is calculated integrating the carrier generation profile as follows:

$$J_{max} = q \int_{300\,nm}^{1200\,nm} \int_{0}^{d_{top,btm}} G(x,\lambda)\,dx d\lambda, \tag{3}$$

where q is the elementary charge, and $d_{\mathrm{top,btm}}$ is the thickness of the top or bottom perovskite layer, respectively.

2.2. Electrical model

In order to model the current/voltage (J/V) characteristics of the tandem cell, we consider each cell to be a pin-type structure, where the current density of each cell is related to the voltage drop across each pin junction through the analytical equation given in [33]. This physical model contains fundamental semiconductor material parameters, and also allows for a straightforward addition of lumped series and shunt resistances to take into account resistive losses. We believe that such model is a good compromise solution between two more extreme possibilities, namely the simple equivalent circuit of the solar cell with very few parameters [34, 35], and the much more detailed numerical models based on the solution of nonlinear differential equations containing the transport and generation/recombination of charge carriers in each perovskite layer [36–39]. The equivalent circuit model is the simplest possible model of a solar cell but lacks applicability in pin solar cells where the photocurrent in general depends on voltage, and cannot be necessarily represented by a constant current–source. In particular, even in high efficiency perovskite solar cells the photocurrent shows a voltage dependence which substantially affects the current/voltage curve [33]. Moreover, many types of perovskite solar cells show hysteresis in the J/V characteristics, which require numerical models that provide a detailed description of ionic transport and ionic trapping/detrapping at the interfaces of the perovskite layer [40]. Fortunately, in the case of highest efficiency perovskite solar cells, as obtained employing defect-engineered perovskites [41], hysteresis is nearly suppressed, enabling simplified analyses. Although the absence of hysteresis does not necessarily rule out the presence of ions, the effect of ions on the J/V curve is in principle reduced to a compensation of the electric field within the perovskite layer, which in standard MAPI cells was shown to be compatible with a reduction of built-in voltage [42, 43]. Such a reduction of the electric field affects the whole J/V curve by reducing charge collection as well as increasing recombination (or dark current). Since in the model adopted here charge collection as well as dark current depend on the electric field, the incorporation of electrostatic compensation by ions is included by taking built-in voltages lower than what would be expected by the difference of work functions of the layers contacting the perovskites.

Further assumptions contained in the analytical model employed here are:

(a) low injection conditions, where the excess carrier density produced by illumination or polarization does not exceed the majority carrier density at each interface of the intrinsic layer,
(b) a linear recombination rate using a lifetime τ,
(c) position independent electron-hole pair photogeneration rate Γ, which is obtained as the spatial mean value of the simulated position-dependent optical generation rate $G(x)$,
(d) symmetric sub-cells, i.e. electrons and holes having identical recombination lifetime τ, mobility μ, and effective interface recombination velocity S at both interfaces of each i-layer.

The electric fields in the intrinsic layers are derived from the built-in voltages of the sub-cells V_{bi} assuming the relative dielectric constant in the perovskites $\varepsilon_{\mathrm{PVK}} = 33.5$, which was measured in MAPI, the intrinsic carrier density n_{i} and assuming that the maximum possible qV_{bi} values correspond to the energy difference of work functions in the materials surrounding the i-layer (see [33] for details). Lower V_{bi} values are also assumed to account for possible field compensation due to interface charging by ions, as discussed above. Due to the lack of experimental data for the intrinsic carrier density in different perovskites, here we estimate n_{i} in an arbitrary perovskite material by taking as reference the value $n_{\mathrm{i,MAPI}} = 6 \times 10^4$ cm^{-3} appropriate for MAPI [33] with the relation

$$n_i = n_{i,MAPI} \exp\left(\frac{E_{g,MAPI} - E_g}{2kT}\right), \tag{4}$$

where $E_{g,MAPI} = 1.58$ eV is the bandgap energy of MAPI, E_g is the bandgap of the perovskite under consideration, k is Boltzmann's constant and $T = 300$ K is the assumed cell temperature. Notice that equation (4) implies that the effective densities of states are assumed equal (see e.g. equation 28 in [44]).

We assume a series-connected tandem solar cell, where the total current of each cell is the same in both the top and the bottom cells, and where the total voltage V is given by the addition $V = V_{top} + V_{btm}$, being V_{top} and V_{btm} the potential difference developed across the top and bottom cells, respectively. Notice that with the series connection, solving for the voltage instead of calculating straightforwardly the current requires a numerical solution using root-finding methods. The values of J are swept across a suitable range in order to repeat the process and obtain the voltage/current curve of each cell, and adding the voltages obtained at each current in each cell to find the total voltage of the tandem cell. Once the current/voltage curve is obtained, the open-circuit voltage V_{OC}, short-circuit current J_{SC}, fill factor FF and efficiency η are calculated.

3. Results

3.1. Optimum light absorption

Not only the thicknesses of the perovskite absorbers have a significant impact on the sunlight absorption and resulting photocurrent, but also the selection of the contact materials, in terms of their complex refractive index, and their thicknesses should be optimized to maximize the photocurrent delivered by both sub-cells and simultaneously comply with the current matching requirement. Given the relatively large number of contact layers used and the wide thicknesses ranges, we used the simulated annealing algorithm, a metaheuristics used to find a global minimum in a large search space [45, 46]. The optimization algorithm was implemented in MATLAB R2018b using the function 'simulannealbnd' of the Global Optimization Toolbox. Two different cases were analyzed: on the one hand, a tandem cell whose contact layers, i.e. transparent conductive oxides (TCO), electron/hole transporting layers (ETL/HTL) and metal back contact, were taken from state of the art cells with experimental efficiencies exceeding 20% [15, 47, 48], and on the other hand, a theoretical ideal tandem cell with just three contact layers, i.e. between glass and top perovskite (front), between both perovskites (middle) and between bottom perovskite and metal contact (back). The layer stack corresponding to the former case, labeled as 'real cell', is shown in figure 1(a), while the stack belonging to the latter, labeled as 'ideal cell', is shown in figure 1(b). In the 'real cell', our optimization problem has as search variables the thicknesses, in the ranges shown in figure 1(a), of the top perovskite absorber and all the contact layers, while the bottom perovskite thickness takes a predefined value. In turn, in the 'ideal cell' it is assumed that the contact layers are perfectly transparent, i.e. $\kappa = 0$ for all wavelengths, and that their thicknesses and refractive index can be freely chosen in the ranges given in figure 1(b). Analogously, the perovskite materials are the same as in the 'real cell' and only the top perovskite thickness is optimized, while the bottom is fixed at a given thickness. For simplicity, it is assumed that the refractive indices of the ideal contact layers are constant over the whole spectral range. The used indices of refraction of state of the art materials can be

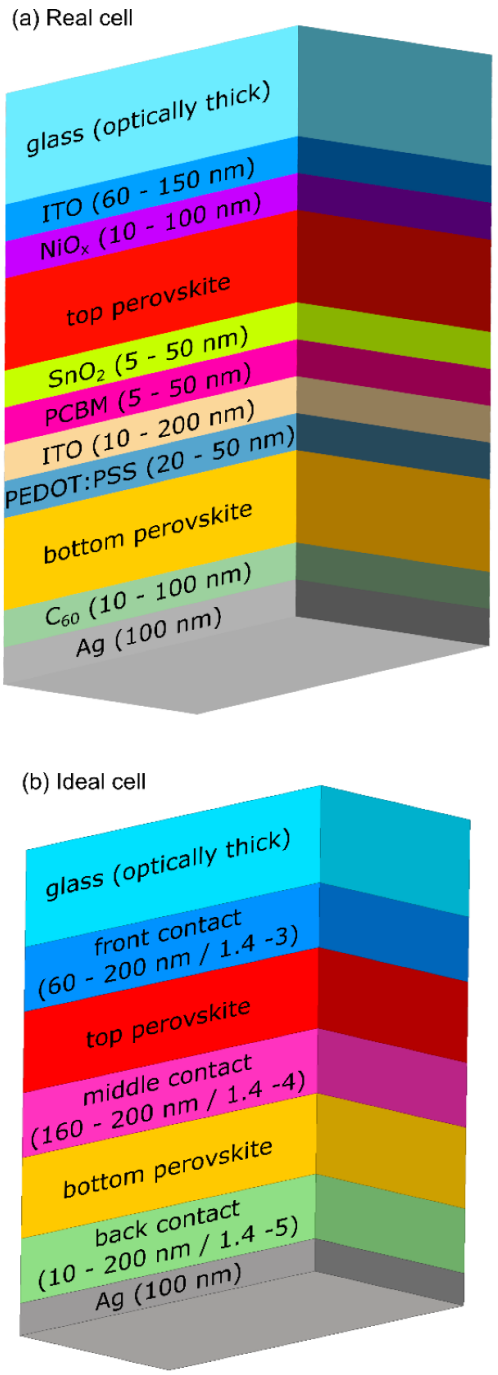

Figure 1. Cell stacks implemented in the optical simulations. The real cell (a) has defined functional layers (PCBM = phenyl-C61-butyric acid methyl ester, PEDOT:PSS = poly(3,4-ethylene dioxythiophene) polystyrene sulfonate), whereas in the ideal cell (b) the perovskite layers are surrounded by perfectly transparent contact layers, whose refractive indices are to be determined through optimization algorithms. Except the thickness of the bottom perovskite, the thickness of each layer is optimized to deliver the highest possible photocurrent under AM1.5G 100 mW cm^{-2} illumination and fulfilling the current matching requirement.

Table 1. Refractive index n values for the front, middle and back layers of the 'ideal cell' case (see figure 1(b)) as a function of the bottom and top perovskite thickness, d_{btm} and d_{top}, respectively. From a solely optical performance perspective, the ideal contact layers are assumed to be perfectly transparent ($\kappa = 0$) and their refractive indices are optimized to yield the maximum photocurrent J_{max} fulfilling the requisite of current matching between both sub-cells.

Layer	d_{btm}	d_{top}	n
	800	499	1.8
Front	500	427	1.9
	300	294	2.0
	800	499	3.1
Middle	500	427	2.6
	300	294	2.0
	800	499	5.0
Back	500	427	3.1
	300	294	1.4

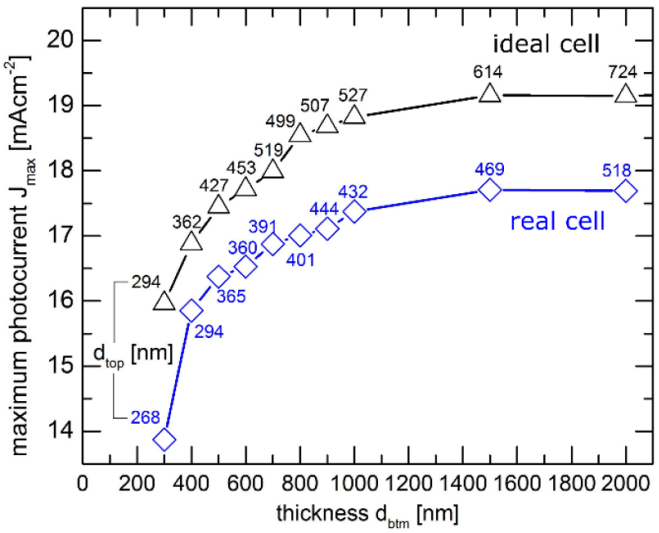

Figure 2. Calculated maximum photocurrent at AM1.5G spectrum irradiation of all-perovskite tandem solar cell connected in series, as a function of the chosen bottom cell perovskite thickness d_{btm}. Diamonds correspond to optimizations using state of the art electron/hole transport layers (ETL/HTL, respectively), while triangles correspond to ideal layers with optimized optical constants that favor optical coupling into the cells. The optical optimization procedure assumes the layer structures depicted in figure 1, using perovskites with gaps $E_{\mathrm{g,top}} = 1.75$ eV and $E_{\mathrm{g,btm}} = 1.17$ eV, with the optimized top cell perovskite thickness d_{top} indicated next to each calculation point.

found in table 3 and figures S1 and S2 of the supplementary information (SI) (stacks.iop.org/JPhysD/53/315104/mmedia) and references therein.

In an actual device, the maximum photocurrent is reduced by recombination and transport losses, yielding the photocurrent $J_{\mathrm{phot}}(V)$, which, more markedly in pin solar cells, depends on the voltage between the terminals of each cell. Thus, $J_{\mathrm{phot}}(V)$ tends to J_{max} at high reverse voltages (provided no shunt losses are present) or when recombination turns negligible in the solar cell. Figure 2 shows the resulting maximum photocurrent J_{max} as a function of the chosen bottom cell thickness d_{btm} for the series-connected tandem solar cell with optimized functional layer thicknesses. The results for the real cell stack of figure 1(a) are shown with diamonds, with the resulting optimum thickness of the top cell d_{top} shown next to each symbol, while triangles represent the results for the ideal cell stack of figure 1(b) and the respective values of d_{top}. The optimized refractive indices and layer thicknesses of the ideal tandem cell for three selected bottom perovskite thicknesses d_{btm} are shown in table 1 and in table SI of the SI, respectively. We notice that the addition of absorbing functional layers in the real cell reduces the attainable photocurrent by 1–2 mA cm^{-2}, regardless of the chosen thickness for the bottom cell. This directly implies a relative efficiency loss of 5%–10% when turning from the ideal to the real device. The results also indicate that in the real cell, d_{top} is between 10% and 30% thinner than in the ideal cell, depending on the value of d_{btm}.

Figure 3 shows the calculated reflectance and absorbance in the (a) 'real' and (b) 'ideal' cells, for a fixed $d_{\mathrm{btm}} = 800$ nm. In the real cell, it was found that the absorbances in the SnO_2, PCBM, the ITO layer between the perovskites, and C_{60} are negligible, and therefore are not shown in figure 3(a). Below each perovskite label the calculated photocurrent is shown and, analogously, the photocurrent loss associated to parasitic absorbance and reflectance is indicated next to each contact layer and reflectance labels, respectively. In the 'ideal cell', the total absorption is especially strong in the visible spectrum, where the reflectance is below 5%. A higher reflectance of 10%–15% is observed in the 300–400 nm spectrum due to an increased reflectance at the air/glass and glass/front contact layer. In turn, in the near-IR spectrum, interference fringes are seen due to weak absorption in the bottom perovskite. The optimized 'real cell' shows a photocurrent of nearly 17 mA cm^{-2}, which is 9% lower than the photocurrent calculated in the 'ideal cell'. This decrease is mainly attributed to parasitic absorbances in the front ITO and PEDOT:PSS layers, as well as an increased overall reflectance, due to non-optimized refractive indices matching of the front contact materials. Advanced light management strategies such as using anti-reflective coatings [49], light diffusers placed on the glass substrates [50, 51], a textured front contact [52] or up/down-converters coatings [53, 54], could further reduce the reflectance in the 300–400 nm range and NIR spectrum, increasing the maximum attainable photocurrent—at a cost of higher manufacturing complexity and time.

3.2. *Influence of optoelectronic parameters*

The electrical output parameters obtained by modeling the $J(V)$ curves according to the model of section 2.2 are obtained using the parameters shown in table 2. The photogeneration rate Γ corresponds to the spatial mean value of the generation rate profile calculated with the optical model at each perovskite layer thickness. Alternatively, it can be calculated from

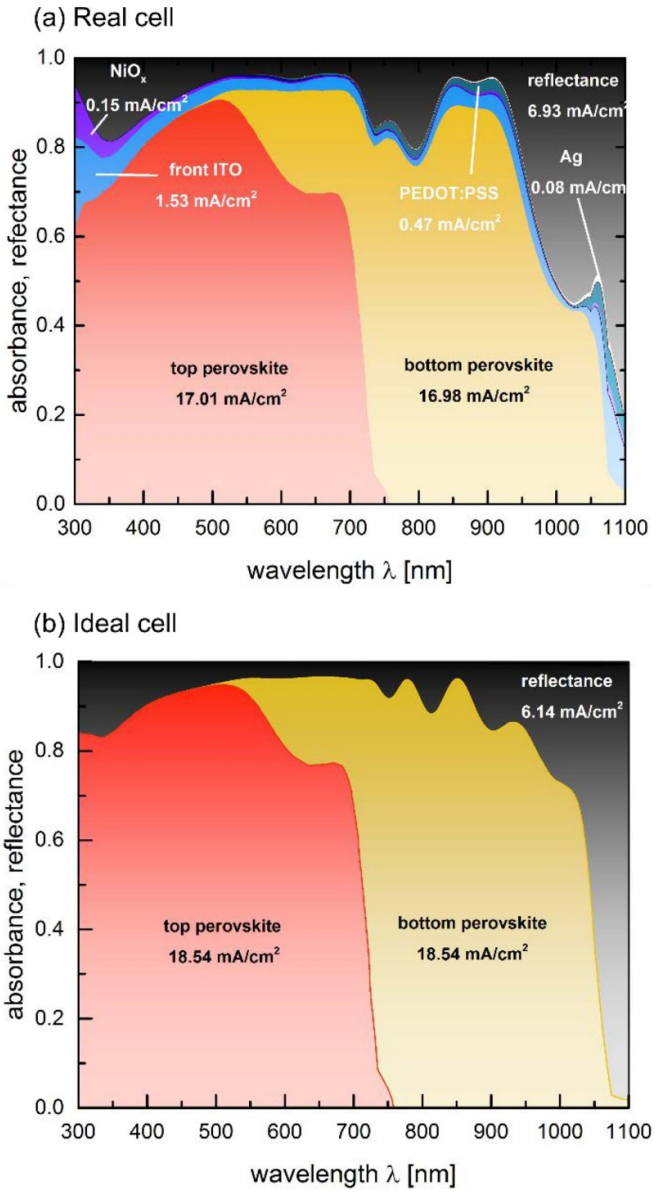

Figure 3. Reflectance (black) and absorbance (various colors) in the (a) 'real' and (b) 'ideal' cells, for a fixed $d_{\mathrm{btm}} = 800$ nm. In the real solar cell, only the main parasitic absorbances are shown: NiO_x, PEDOT:PSS, ITO and Ag. Next to each label are shown the values obtained for the attainable photocurrent (in the perovskite layers) and the photocurrent losses (in all other layers).

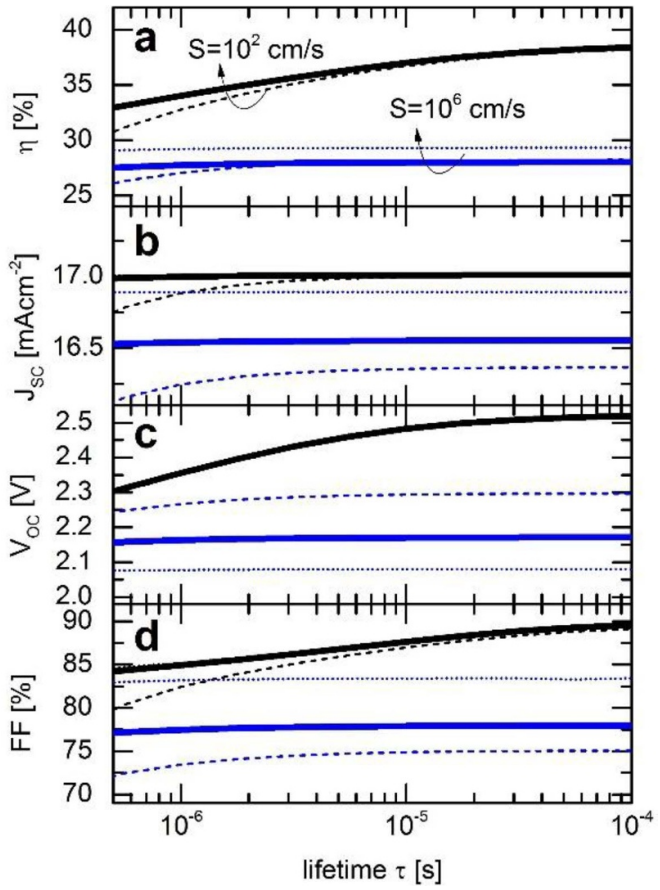

Figure 4. Calculated efficiency η, short circuit current density J_{SC}, open circuit voltage V_{OC} and fill factor FF for a series–connected perovskite–perovskite tandem cell with top and bottom gaps $E_{\mathrm{g,top}} = 1.17$ eV, $E_{\mathrm{g,btm}} = 1.75$ eV, and absorber thicknesses of $d_{\mathrm{top}} = 401$ nm, $d_{\mathrm{btm}} = 800$ nm. Blue and black curves correspond to low and high interface recombination velocities of $S = 10^2$ cm s^{-1} and $S = 10^6$ cm s^{-1}, respectively. The different line type in each curve set corresponds to different mobilities μ: 10^{-1} cm^2 V^{-1} s^{-1} (dashed), 10^0 cm^2 V^{-1} s^{-1} (solid) and 10^1 cm^2 V^{-1} s^{-1} (dotted). With the chosen near-optimum bandgaps of existing perovskites, conversion efficiencies above 30% are attainable only with low interface recombination velocities.

$\Gamma_{\mathrm{top,btm}} = J_{\mathrm{max}}/qd_{\mathrm{top,btm}}$, where the subscripts 'top,btm' indicate the corresponding perovskite.

An additional parameter not contained in table 2 is the series resistance, which is only utilized and explicitly indicated in the last study, shown in section 3.2.4. All other results shown in this subsection assume no series resistance effects.

3.2.1. Carrier mobility and lifetime. Figure 4 gives the (a) simulated power conversion efficiency η, (b) short circuit current density J_{SC}, (c) open–circuit voltage V_{OC} and (c) fill factor FF for a tandem cell as a function of lifetime τ (x-axis) and mobilities $\mu = 10^{-1}$ cm^2 Vs^{-1} (dashed), $\mu = 10^0$ cm^2 Vs^{-1} (solid) and $\mu = 101$ cm^2 Vs^{-1} (dotted). The range of lifetime values chosen here covers the range of experimental values obtained by different direct and indirect methods in various perovskites [33, 55, 56]. The corresponding photogeneration rates are calculated according to the optimization of the layer structure of figure 1(a) for $d_{\mathrm{btm}} = 800$ nm and $d_{\mathrm{top}} = 401$ nm. All three parameters, namely τ, μ and S, are assumed equal in the bottom and top cells. Two sets of curves distinguish between high interface recombination velocity $S = 10^6$ cm s^{-1} (blue), and low interface recombination $S = 10^2$ cm s^{-1} (black). In the case where $S = 10^2$ cm s^{-1} (black), the dotted lines corresponding to the highest mobility are not seen because they overlap with the thick solid lines where $\mu = 10^0$ cm^2 Vs^{-1}. The results shown in figure 4 reveal that tandem cells with material parameters present in state of the art perovskites and optimized layer thicknesses, device efficiencies well around 30% should be feasible. According to our

Table 2. Values or ranges of different material parameters utilized to compute the current-voltage characteristics at room temperature.

Parameter	Bottom cell	Top cell
Perovskite	$CH_3NH_3Sn_{0.85}Pb_{0.15}I_3$	$Cs_{0.08}FA_{0.02}PbI_{2.31}Br_{0.61}Cl_{0.08}$
Bandgap E_g (eV)	1.17	1.75
Relative dielectric constant ε_{PVK}	33.5	33.5
Intrinsic carrier concentration n_i (cm^{-3})	1.66×10^8	2.24×10^3
Photogeneration rate Γ	Depends on thickness	Depends on thickness
Minority carrier lifetime τ (s)	5×10^{-7}–10^{-4}	5×10^{-7}–10^{-4}
Carrier mobility μ ($cm^2\ V^{-1}\ s^{-1}$)	10^{-1}–10^2	10^{-1}–10^2
Interface recombination velocity S ($cm\ s^{-1}$)	10^0–10^6	10^0–10^6
Built-in voltage V_{bi} (V)	0.585–1.17	0.875–1.75

results, the mandatory requisite to surpass 30% efficiency is to achieve low interface recombination velocities below 10^2 cm s^{-1}, including series resistance effects (see below). Such low recombination velocities seem feasible within a range of preparation methods and contact layer materials, as shown by different photoluminescence measurements and model fits on different perovskite solar cells [33, 56, 57]. In subsection 3.2.3 interface recombination effects are studied in more detail.

Notice also that mobility plays a much more important role when high interface recombination is present (blue curves in figure 4). A higher mobility enhances the short circuit current and fill factor, due to a higher current at the maximum power point (not shown in figure 4). Contrarily, higher mobility reduces the open circuit voltage, since carriers reach more likely the high recombination interfaces than with a lower mobility [55].

3.2.2. Dependence on built-in voltage. The previous calculations assume the ideal situation where the built–in voltage in each perovskite layer equals the bandgap, i.e. $qV_{bi,btm} = E_{g,btm}$ and $qV_{bi,top} = E_{g,top}$. The prospects of reaching these conditions in practice are likely, in view of the diverse experimental surface modification methods available for the tuning of the work function of contact materials (see, e.g. the case of C_{60} [56], TiO_2 [57], SnO_2 [58] and spiro-OMeTAD [59]). Nevertheless, since the built–in voltage can be severely reduced by ion accumulation at inappropriate interfaces [42], it seems appropriate to quantify the incidence of $V_{bi,btm}$ and $V_{bi,top}$ on the efficiency of the tandem cell. Obeying a high efficiency criterion, here we choose $d_{btm} = 800$ nm and $d_{top} = 401$ nm, interface recombination velocities of $S = 10^2$ cm s^{-1} in all perovskite interfaces, and a diffusion length $L = 1600$ nm, obtained with $\mu = 1$ $cm^2\ V^{-1}\ s^{-1}$ and $\tau = 1$ μs, exceeding the thickness of each perovskite layer. According to the results shown in figure 4, these parameter values enable efficiencies well over 30% with built-in voltages matching the bandgaps.

Figure 5 shows the calculated efficiency varying each built–in voltage between half the value of the corresponding bandgap (begin of each axis) and the value of the bandgap (end of each axis). In the studied range, the built-in voltage of the top cell has a stronger incidence on efficiency than the built-in voltage of the bottom cell. In order to exceed 30% efficiency under these conditions, it can be seen from figure 5 that $qV_{bi,top}$ must exceed $0.5 \times E_{g,top}$ by at least 300 mV. Notice, from figure 5, that the efficiency gains obtained by increasing the built–voltage slow down when approaching the highest V_{bi} values.

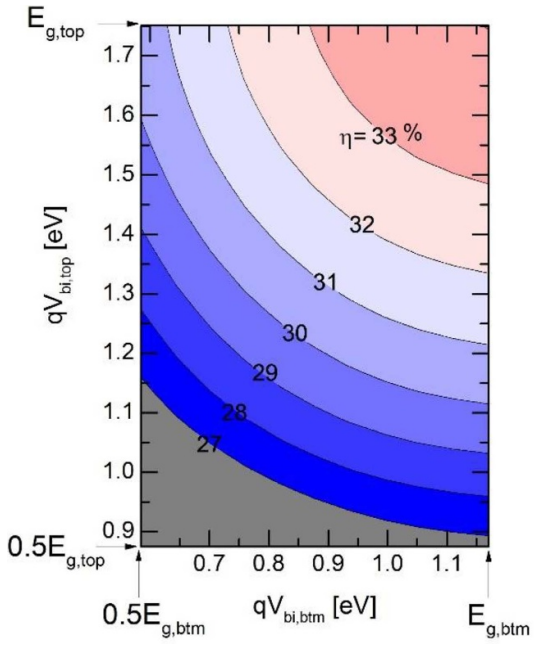

Figure 5. Calculated tandem cell efficiency depending on the built-in voltage of the top $V_{bi,top}$ and bottom $V_{bi,btm}$ cells, respectively. The calculations assume recombination velocities at contacts of $S = 10^2$ cm s^{-1} in the top and bottom cells, mobilities of $\mu = 1$ $cm^2\ V^{-1}\ s^{-1}$ and minority carrier lifetimes of $\tau = 1$ μs. Efficiency increases when both the top and bottom built-in voltages approach the maximum value corresponding to each perovskite bandgap, with a larger incidence of the built-in voltage of the top (larger bandgap) solar cell. Efficiencies above 30% require that the built-in voltage of the cell with larger gap is at least 300 mV higher than half the bandgap.

3.2.3. Different interface recombination velocities in top/bottom cells. In section 3.2.2 we noticed that the interface recombination affects strongly the efficiency of the tandem solar cell, finding that high interface recombination velocities of 10^6 cm s^{-1} prevent the solar cell from reaching 30% efficiency, even at the highest considered mobilities and minority carrier recombination lifetimes. In this subsection we investigate the influence of interface recombination in

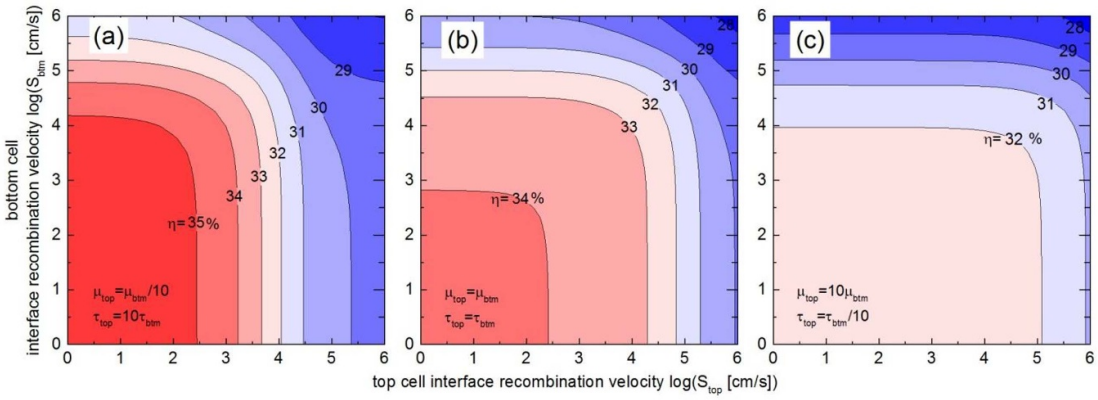

Figure 6. Dependence of cell efficiency (values indicated on each contour line) as a function of bottom/top cell interface recombination velocity $S_{\mathrm{btm,top}}$, respectively. The calculations use the perovskite thicknesses $d_{\mathrm{btm}} = 800$ nm, $d_{\mathrm{top}} = 401$ nm (see figure 2). The mobility and lifetime of the top cell varies from (a) (low μ_{top}, high τ_{top}) to (c) (high μ_{top}, low τ_{top}), keeping the diffusion length constant.

more detail, allowing for different recombination velocities at the interfaces of the top and bottom cells. The influence of interface recombination is ensured by selecting $\mu\tau$ products corresponding to diffusion lengths that exceed each cell thickness, concomitantly corresponding to our criterion of finding conditions for high efficiency cells. Therefore, we choose mobility and lifetime values in the top and bottom cells meeting the respective ratios $L_{\mathrm{top}}/d_{\mathrm{top}} = 4$ and $L_{\mathrm{btm}}/d_{\mathrm{btm}} = 2$ with thickness values $d_{\mathrm{btm}} = 800$ nm, $d_{\mathrm{top}} = 401$ nm. Figure 6 shows the calculated efficiencies of tandem cells having interface recombination velocities S_{top}, S_{btm}, obtained with bottom cell parameters $\mu_{\mathrm{btm}} = 1$ cm^2 V^{-1} s^{-1} and $\tau_{\mathrm{btm}} = 1$ μs, and the following top cell parameter combinations: $\mu_{\mathrm{top}} = \mu_{\mathrm{btm}}/10$, $\tau_{\mathrm{top}} = 10 \times \tau_{\mathrm{btm}}$ in plot (a), $\mu_{\mathrm{top}} = \mu_{\mathrm{btm}}$, $\tau_{\mathrm{top}} = \tau_{\mathrm{btm}}$ in plot (b), and $\mu_{\mathrm{top}} = 10 \times \mu_{\mathrm{btm}}$, $\tau_{\mathrm{top}} = \tau_{\mathrm{btm}}/10$ in plot (c).

In general, for all three plots, efficiencies clearly above 30% become accessible if one of both cells interfaces show moderate ($\sim 10^4$ cm s^{-1}) recombination velocities. Remarkably, it is not mandatory that both cells have low interface recombination simultaneously to reach efficiencies higher than 30%. Furthermore, having unequal mobilities and lifetimes in the top and bottom cells may yield higher efficiencies than the tandem cell with balanced carrier transport properties (figure 6(b)).

The region of figure 6(a) with $S_{\mathrm{top}} < 10^3$ cm s^{-1} shows higher efficiency than the case of equal parameters of figure 6(b) because of the tenfold higher lifetime. The higher lifetime implies higher fill factor and open circuit voltage, and the lower mobility of this case does not impact significantly the photocurrent at short circuit, resulting in a 1% absolute efficiency enhancement. With high mobility and low lifetime required to maintain the diffusion length (figure 6(c)), the open circuit voltage and fill factor limit the overall efficiency of the tandem cell to 32% regardless of the low interface recombination velocities.

The results shown in figures 6(a)–(c) assume the ideal case of no series resistance. When performing calculations with a series resistance of 2 Ω cm^2, the overall efficiency levels seen in figure 6 are reduced by approximately 2% absolute, and the trends observed in figure 6 remain unchanged. The following section inspects further the influence of series resistance.

3.2.4. Dependence on thickness and series resistance. Since J_{max} increases beyond $d_{\mathrm{btm}} = 800$ nm (cf Figure 2), it seems meaningful to calculate the efficiencies also at higher thickness values, even if in principle it seems unfeasible to prepare such thick layers with good quality using current preparation techniques. Notice that although higher d_{bot} ensures higher J_{max}, the actual photocurrent J_{phot} in a pin solar cell depends not only on transport and recombination losses, but also on the electric field within the i-layer. Since a given set of contact materials establishes the built-in voltage in the perovskite absorber, the electric field in equilibrium increases in thinner cells, favoring photocarrier collection, resulting in an increased efficiency. Furthermore, lower thickness favors higher open circuit voltage values and fill-factor, provided recombination velocity at the interfaces between the perovskite and contacts is moderate to low ($<10^3$ cm s^{-1}) [60]. Both observations lead to the possibility of higher efficiencies at absorber thickness that are below the optically calculated optimum thickness values. From a fabrication point of view, lower thicknesses imply in principle lower processing times and material consumption, although a higher probability of pinhole formation and thus smaller shunt resistance [61]. So far we adopted a bottom cell thickness of $d_{\mathrm{btm}} = 800$ nm, as a compromise between maximization of light absorption and maximum layer thickness constrained by state of the art preparation methods. Here, we explore the electrical output parameters in the whole range of d_{btm} from 300 nm to 2000 nm, disregarding possible thickness limitations imposed by current preparation methods.

The optical optimization through a careful selection of contact layers bears a large benefit for tandem efficiency. Figure 7 shows the calculated output parameters of the tandem cell with the real (blue symbols) and ideal (black symbols) contact layers optimized following the optical optimization of section 2.1. At given bottom cell thickness above 400 nm, optimum contact layers yield 1 mA cm^{-2} increase in photocurrent (figure 7(b)) with a potential efficiency improvement between 6% to 8% relative (figure 7(a)), independently of the impact of series resistance. Conversely, at a given efficiency level, e.g. $\eta = 34\%$ (dashed line in figure 7(a)), the adoption of optically

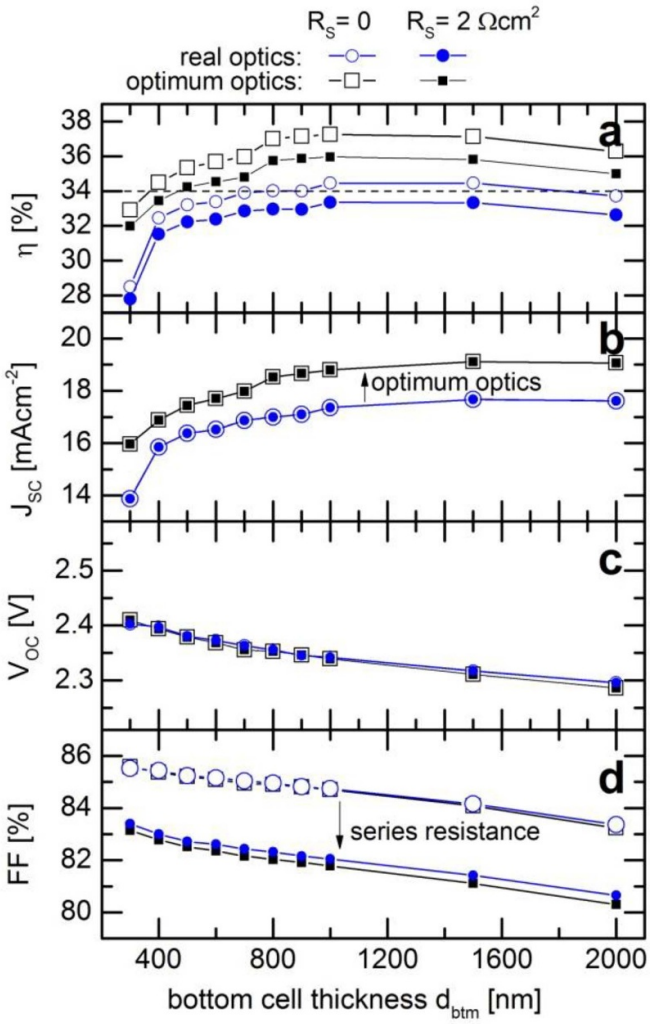

Figure 7. (a) Calculated efficiency η, (b) short circuit current density J_{SC}, (c) open circuit voltage V_{OC} and (d) fill factor FF for a series–connected all-perovskite tandem cell as a function of the thicknesses of the bottom perovskite d_{btm}, with the thickness of the top perovskite following the optimum values of figure 2. The calculations are performed for the ideal case where all contact layers have optimum optical constants and thicknesses (black symbols), and the case of a cell with real optical indices for the ETL and HTL layer (blue symbols, see text for details). Each case is calculated without series resistance and with a series resistance of $R_S = 2\ \Omega\ cm^2$, representing a high series resistance situation. The interface recombination in both cells are set to $S = 10^2$ cm s^{-1}, all carrier mobilities to $\mu = 1\ cm^2\ V^{-1}\ s^{-1}$, and recombination lifetimes $\tau = 1\ \mu s$.

ideal contact layers allows a reduction in bottom cell thickness by a factor larger than 2, e.g. from 1000 nm to 400 nm.

4. Towards minimum-loss contact layers

Many contact layers were already investigated to improve the efficiency of single junction perovskite solar cells [16–18], focusing not only in the alignment of energy levels with the perovskite energy bands, but also in the development of low temperature deposition methods for perovskite capping layers. In order to achieve the highest efficiencies in tandem perovskite cells, these contact layers must have good electronic properties as well as optical characteristics suitable for the optical optimization presented in section 2.1. Recalling table 1, the optimized thicknesses and refractive indices of the contact layers in the 'ideal cell' depend strongly on the bottom perovskite thickness d_{btm}. In this ideal case, the optimization assumes that each contact layer, namely front, middle and back, is a single homogeneous material, disregarding the fact that in practice, each layer may be a compound of more than one material layer (e.g. a front layer composed by a transparent conductive material and a HTL). Furthermore, this idealization assumes for simplicity that the real part of the refractive index n is constant in the whole wavelength range, although real materials show a wavelength dependence.

Table 3. Refractive index range of selected materials. Superscripts represent the wavelength ranges where n values were taken: a: 300–1100 nm, b: 300–900 nm, c: 400–1100 nm. The rightmost column indicates the potential function as a contact layer in the tandem cell.

Material	Refractive index range (n_{min}–n_{max})	Function
Transparent conductive layer		
FTO [57]	1.6–2.3[a]	Front
ITO [58]	1.3–2.4[a]	Front, middle
AZO [59]	1.6–2.3[b]	Front, middle
IZO [60]	1.8–2.0[c]	Front, middle
Hole transport layer		
NiO_x [61]	1.9–2.1[a]	Front, middle
CuSCN [62]	1.9–2.3[b]	Front, middle
MoO_3 [66]	1.8–2.2[b]	Front, middle
P3HT [67]	1.9–2.4[a]	Front, middle
PEDOT:PSS [68]	1.4–1.7[b]	Front, middle
Electron transport layer		
SnO_2 [69]	1.8–2.0[a]	Middle, back
C_{60} [70]	2.0–2.4[a]	Middle, back
PCBM [68]	1.9–2.2[b]	Middle, back

Refractive indices for some of the materials commonly used as TCO, HTLs and ETLs are presented in table 3, showing their minimum and maximum values, n_{min} and n_{max} respectively, for the wavelength range between 300 nm and 1200 nm. While some materials like NiO_x and CuSCN (copper thiocyanate) have a decreasing dependence of n with wavelength, the majority of organic materials show non monotonic curves (see figure S1 of SI). From the optical optimization perspective, a criterion to select contact layers for tandem solar cells is that the ideal n values shown in table 1 are contained in the range (n_{min}, n_{max}) of a chosen real material. For the front contact, all HTL and TCO materials presented in table 3 fit this criterion, with the exception of PEDOT:PSS. For the middle layer, TCO, HTL and ETL materials have n ranges that contain the ideal n, but only for $d_{btm} = 300$ nm. For the back layer, the ideal n lies outside the ranges for all the selected materials. However, it is expected that the impact of this layer in the optical performance will be negligible, because

eventually nearly all the radiation that passes through the back layer will be reflected back at the Ag contact.

As stated above, the optimization with ideal contact layers assumes they are perfectly transparent, i.e. $\kappa = 0$. In real materials, the non-zero values of κ lead to parasitic absorption which can reduce drastically the photocurrent and the device efficiency, as was mentioned in section 3.1. Figure S2 in the SI shows a comparison between absorption coefficients α of real contact materials listed in table 3 and the perovskites used throughout this work. The comparison is made in the wavelength ranges where each layer can have a significant impact, assuming that the perovskite absorbs all the wavelengths below its bandgap.

Together with the optical constants, the energy alignment between perovskites and contact layers needs to be considered for a proper material selection. Although the bulk electron affinity and work function of materials may serve as a starting point to select the contact materials sandwiching each perovskite layer, they cannot be used rigorously as a material selection criterion, since their values are very sensitive to preparation and post-processing methods [62]. Therefore, in principle we can assume that all the materials listed in table 3 are potentially applicable to the proposed tandem configuration.

Following the guidelines discussed so far, it is next proposed to interchange the PEDOT:PSS and middle ITO layers, with the materials CuSCN and AZO, respectively, for the stack of figure 1(a), and optimize the new stack with a fixed bottom perovskite thickness of $d_{\mathrm{btm}} = 300$ nm. As it can be seen in the tables 1 and 3, these materials modifications should imply an improvement in the light absorption since the refractive indices of CuSCN and AZO are closer to the ideal ones. The optimization algorithm gives a maximum photocurrent $J_{\mathrm{max}} = 15.45$ mA cm^{-2} for this alternative cell, which is 11% higher than the photocurrent delivered by the original stack configuration and approaches the value $J_{\mathrm{max}} = 15.96$ mA cm^{-2} of the ideal cell (see figure 2 with $d_{\mathrm{btm}} = 300$ nm). Consequently, with the enhanced $J_{\mathrm{max}} = 15.45$ mA cm^{-2}, the electrical model predicts that the efficiency of the optimized alternative cell reaches 32% (see figure 7(a), with $d_{\mathrm{btm}} = 300$ nm), representing an improvement of 14% (relative) to the initial efficiency. The optimized thicknesses of this tandem cell are listed in the Table S1 of the SI under the label 'Alternative'.

5. Conclusions

In this contribution we have combined a well-established optical model based on the generalized transfer matrix approach with a drift-diffusion analytical current/voltage characteristics to model two-terminal all-perovskite tandem cells. From the simulations, a deeper insight into the impact of optoelectronic parameters on the electrical output parameters was obtained. For instance, it was observed that the surface recombination velocity at the perovskite/contact interfaces is a major limiting factor to obtain tandem cells with efficiencies clearly above 30%. Interestingly, unbalanced electronic transport properties between the top and bottom cells can have even a positive effect on the device efficiency compared to perovskite absorbers with identical properties.

The optical optimization allows us to identify the contact layers that have a large contribution to the parasitic absorbance and photocurrent loss. Furthermore, the optimization algorithm can provide guidelines to select not only the optimum thickness for all the contact layers but also the optimum materials, based on their refractive index, to avoid reflectance and maximize sunlight absorption in the perovskites.

The simulations results suggest that in order to achieve tandem cells with efficiencies above 30% the device should comply with the following requirements:

- Photocurrent losses associated to parasitic absorbances and reflectance lower than 2 mA cm^{-2} and 7 mA cm^{-2}, respectively, to ensure a maximum photocurrent not lower than 16 mA cm^{-2}.
- A modest ($\sim 10^4$ cm s^{-1}) to low ($\sim 10^2$ cm s^{-1}) surface recombination velocity at the perovskite/contact interfaces in both sub-cells.
- A mobility-lifetime product on the order of 10^{-6} cm^2 V^{-1}, which implies a diffusion length of $\sim$1500 nm, surpassing the perovskite thickness.
- Built-in voltages corresponding to at least 300 mV above half the bandgap.
- Series resistances not higher than 2 Ω cm^2.

We would like to emphasize that these requisites are fulfilled by current high-performing perovskites and single junction solar cells based on such materials. The difficulty is therefore to concomitantly comply with these requirements in both perovskite sub-cells stacked as a monolithically tandem cell. Especially challenging is to obtain a low-bandgap perovskite ($E_{\mathrm{g}} \sim 1.2$ eV) with good electronic transport properties similar to state of the art MAPI or triple cation perovskites, and therefore this should be the main task for community efforts aiming at high efficiency tandem cells.

Acknowledgments

M S would like to thank the Alexander von Humboldt Foundation and Professor A Lasagni (TU Dresden) for supporting this work.

Appendix

In the following, the current J–voltage V equation derived originally in [22] and used throughout this work is presented. The electric field F in the intrinsic perovskite layer with thickness d is given by

$$F = (V - V_0)/d, \tag{5}$$

where the voltage drops at the perovskite interfaces reduce the built-in voltage V_{bi} to the voltage V_0 given by

$$V_0 = V_{bi} - 4V_t - 2V_t W\left(\frac{1}{2}\left(\frac{V_t d}{V_{bi}L_i}\right)^2 e^{\frac{V_{bi}}{2V_t}}\right), \quad (6)$$

where W is the Lambert-W function, $V_t = kT/q$ is the thermal voltage (k is Planck's constant, T is temperature and q is the fundamental charge), L_i is the dielectric Debye–Hückel length of the intrinsic semiconductor given by $L_i = \sqrt{\varepsilon V_t/(2qn_i)}$, with ε the semiconductor permittivity and n_i the intrinsic carrier concentration. The physical assumptions and electronic parameters corresponding to perovskite semiconductors and solar cells are described in detail in [33]. The JV equation obtained with the drift/diffusion model for p-i-n cells is

$$J(V) = J_{dark}(V) - J_{ph}(V), \quad (7)$$

where $J_{ph}(V)$ is the photocurrent density

$$J_{ph}(V) = J_{max}F_c(V), \quad (8)$$

where J_{max} is the maximum photocurrent and the voltage-dependent global collection efficiency $F_c(V)$ is given by

$$F_c(V) = 2\left(\frac{L}{d}\right)^2 \times \left\{(\beta_1+\beta_2)\frac{1+\left(\frac{\beta_1-\beta_2-Sd/D}{\beta_2+Sd/D}\right)e^{-\frac{\beta_1}{2}}}{1+\left(\frac{\beta_1-Sd/D}{\beta_2+Sd/D}\right)e^{-\frac{\beta_1+\beta_2}{2}}} - \beta_1\right\}. \quad (9)$$

The effective diffusion coefficient D is obtained from the effective mobility μ using Einstein's relation $D = V_t\mu$, whereas the effective diffusion length is given by $L = \sqrt{D\tau}$ with τ the carrier effective lifetime. The dimensionless quantities β_1 (plus sign) and β_2 (minus sign) are given by

$$\beta_{1,2} = \sqrt{\left(\frac{d}{L}\right)^2 + \left(\frac{V-V_0}{2V_t}\right)^2} \pm \left(\frac{V-V_0}{2V_t}\right). \quad (10)$$

The dark current density is given by

$$J_{dark}(V) = J_0(V) \times \left(e^{\frac{V}{2V_t}} - 1\right), \quad (11)$$

where J_0 is the voltage dependent reverse saturation current density given by

$$J_0(V) = \frac{2qn_iD}{d} \times \left(\beta_1 + \frac{\beta_1+\beta_2}{\left(\frac{Sd/D+\beta_2}{Sd/D-\beta_1}\right)e^{\frac{\beta_1+\beta_2}{2}} - 1}\right). \quad (12)$$

ORCID iD

Marcos Soldera https://orcid.org/0000-0002-3990-5187

References

[1] Green M A, Dunlop E D, Levi D H, Hohl-Ebinger J, Yoshita M and Ho-Baillie A W Y 2019 Solar cell efficiency tables (version 54) *Prog. Photovolt. Res. Appl.* **27** 565–75

[2] Green M A, Ho-Baillie A and Snaith H J 2014 The emergence of perovskite solar cells *Nat. Photon.* **8** 506–14

[3] Stranks S D, Eperon G E, Grancini G, Menelaou C, Alcocer M J, Leijtens T, Herz L M, Petrozza A and Snaith H J 2013 Electron-hole diffusion lengths exceeding 1 micrometer in an organometal trihalide perovskite absorber *Science* **342** 341–4

[4] Steirer K X, Schulz P, Teeter G, Stevanovic V, Yang M, Zhu K and Berry J J 2016 Defect tolerance in methylammonium lead triiodide perovskite *ACS Energy Lett.* **1** 360–6

[5] Eperon G E, Stranks S D, Menelaou C, Johnston M B, Herz L M and Snaith H J 2014 Formamidinium lead trihalide: a broadly tunable perovskite for efficient planar heterojunction solar cells *Energy Environ. Sci.* **7** 982–8

[6] Brenner T M, Egger D A, Kronik L, Hodes G and Cahen D 2016 Hybrid organic–inorganic perovskites: low-cost semiconductors with intriguing charge-transport properties *Nat. Rev. Mater.* **1** 15007

[7] Sha W E I, Ren X, Chen L and Choy W C H 2015 The efficiency limit of $CH_3NH_3PbI_3$ perovskite solar cells *Appl. Phys. Lett.* **106** 221104

[8] Hirst L C and Ekins-Daukes N J 2011 Fundamental losses in solar cells *Prog. Photovolt. Res. Appl.* **19** 286–93

[9] Ahn N, Son D-Y, Jang I-H, Kang S M, Choi M and Park N-G 2015 Highly reproducible perovskite solar cells with average efficiency of 18.3% and best efficiency of 19.7% fabricated via Lewis base adduct of lead (II) iodide *J. Am. Chem. Soc.* **137** 8696–9

[10] Yang W S *et al* 2017 Iodide management in formamidinium-lead-halide-based perovskite layers for efficient solar cells *Science* **356** 1376–9

[11] Saliba M *et al* 2016 Cesium-containing triple cation perovskite solar cells: improved stability, reproducibility and high efficiency *Energy Environ. Sci.* **9** 1989–97

[12] Nogay G, Sahli F, Werner J, Monnard R, Boccard M, Despeisse M, Haug F-J, Jeangros Q, Ingenito A and Ballif C 2019 25.1%-efficient monolithic perovskite/silicon tandem solar cell based on a p-type monocrystalline textured silicon wafer and high-temperature passivating contacts *ACS Energy Lett.* **4** 844–5

[13] Yoshikawa K *et al* 2017 Silicon heterojunction solar cell with interdigitated back contacts for a photoconversion efficiency over 26% *Nat. Energy* **2** 17032

[14] Tong J, Song Z, Kim D H, Chen X, Chen C, Palmstrom A F, Ndione P F, Reese M O, Dunfield S P and Reid O G 2019 Carrier lifetimes of > 1 μs in Sn–Pb perovskites enable efficient all-perovskite tandem solar cells *Science* **364** 475–9

[15] Hörantner M T, Leijtens T, Ziffer M E, Eperon G E, Christoforo M G, McGehee M D and Snaith H J 2017 The potential of multijunction perovskite solar cells *ACS Energy Lett.* **2** 2506–13

[16] Mahmood K, Sarwar S and Mehran M T 2017 Current status of electron transport layers in perovskite solar cells: materials and properties *RSC Adv.* **7** 17044–62

[17] Calio L, Kazim S, Grätzel M and Ahmad S 2016 Hole-transport materials for perovskite solar cells *Angew. Chem. Int. Ed.* **55** 14522–45

[18] Ameen S, Rub M A, Kosa S A, Alamry K A, Akhtar M S, Shin H-S, Seo H-K, Asiri A M and Nazeeruddin M K 2016 Perovskite solar cells: influence of hole transporting materials on power conversion efficiency *ChemSusChem* **9** 10–27

[19] Burkhard G F, Hoke E T, Scully S R and McGehee M D 2009 Incomplete exciton harvesting from fullerenes in bulk heterojunction solar cells *Nano Lett.* **9** 4037–41

[20] Jung S, Kim K-Y, Lee Y-I, Youn J-H, Moon H-T, Jang J and Kim J 2011 Optical modeling and analysis of organic solar cells with coherent multilayers and incoherent glass substrate using generalized transfer matrix method *Japan J. Appl. Phys.* **50** 122301

[21] Pettersson L A A, Roman L S and Inganas O 1999 Modeling photocurrent action spectra of photovoltaic devices based on organic thin films *J. Appl. Phys.* **86** 487–96

[22] Taretto K 2012 New explicit current/voltage equation for p-i-n solar cells including interface potential drops and drift/diffusion transport *Prog. Photovolt. Res. Appl.* **22** 870–84

[23] Liao W *et al* 2016 Fabrication of efficient low-bandgap perovskite solar cells by combining formamidinium tin iodide with methylammonium lead iodide *J. Am. Chem. Soc.* **138** 12360–3

[24] Yang Z, Rajagopal A, Chueh C-C, Jo S B, Liu B, Zhao T and Jen A K-Y 2016 Stable low-bandgap Pb–Sn binary perovskites for tandem solar cells *Adv. Mater.* **28** 8990–7

[25] Zhao D *et al* 2017 Low-bandgap mixed tin–lead iodide perovskite absorbers with long carrier lifetimes for all-perovskite tandem solar cells *Nat. Energy* **2** 17018

[26] Werner J, Nogay G, Sahli F, Yang T C-J, Bräuninger M, Christmann G, Walter A, Kamino B A, Fiala P and Löper P 2018 Complex refractive indices of cesium–formamidinium-based mixed-halide perovskites with optical band gaps from 1.5 to 1.8 eV *ACS Energy Lett.* **3** 742–7

[27] Anaya M *et al* 2016 Optical analysis of $CH_3NH_3Sn_xPb_{1-x}I_3$ absorbers: a roadmap for perovskite-on-perovskite tandem solar cells *J. Mater. Chem.* A **4** 11214–21

[28] van Eerden M, Jaysankar M, Hadipour A, Merckx T, Schermer J J, Aernouts T, Poortmans J and Paetzold U W 2017 Optical analysis of planar multicrystalline perovskite solar cells *Adv. Opt. Mater.* **5** 1700151

[29] Kang K, Lee S and Kim J 2013 Effect of an incoherent glass substrate on the absorption efficiency of organic solar cells at oblique incidence analyzed by the transfer matrix method with a glass factor *Japan J. Appl. Phys.* **52** 052301

[30] Eperon G E *et al* 2016 Perovskite-perovskite tandem photovoltaics with optimized band gaps *Science* **354** 861

[31] Zhao D *et al* 2018 Efficient two-terminal all-perovskite tandem solar cells enabled by high-quality low-bandgap absorber layers *Nat. Energy* **3** 1093–100

[32] Leijtens T *et al* 2018 Tin–lead halide perovskites with improved thermal and air stability for efficient all-perovskite tandem solar cells *Sustain. Energy Fuels* **2** 2450–9

[33] Taretto K, Soldera M and Koffman-Frischknecht A 2017 Material parameters and perspectives for efficiency improvements in perovskite solar cells obtained by analytical modeling *IEEE J. Photovolt.* **7** 206–13

[34] Chan D S H and Phang J C H 1987 Analytical methods for the extraction of solar-cell single- and double-diode model parameters from I–V characteristics *IEEE Trans. Electron Devices* **34** 286–93

[35] Miyano K, Yanagida M, Tripathi N and Shirai Y 2015 Simple characterization of electronic processes in perovskite photovoltaic cells *Appl. Phys. Lett.* **106** 093903

[36] Miyano K, Tripathi N, Yanagida M and Shirai Y 2016 Lead halide perovskite photovoltaic as a model p–i–n diode *Acc. Chem. Res* **49** 303–10

[37] Liu F, Zhu J, Wei J, Li Y, Lv M, Yang S, Zhang B, Yao J and Dai S 2014 Numerical simulation: toward the design of high-efficiency planar perovskite solar cells *Appl. Phys. Lett.* **104** 253508

[38] Zhou Y and Gray-Weale A 2016 A numerical model for charge transport and energy conversion of perovskite solar cells *Phys. Chem. Chem. Phys.* **18** 4476–86

[39] Neukom M T *et al* 2019 Consistent device simulation model describing perovskite solar cells in steady-state, transient, and frequency domain *ACS Appl. Mater. Interfaces* **11** 23320–8

[40] Lopez-Varo P, Jiménez-Tejada J A, García-Rosell M, Ravishankar S, Garcia-Belmonte G, Bisquert J and Almora O 2018 Device physics of hybrid perovskite solar cells: theory and experiment *Adv. Energy Mater.* **8** 1702772

[41] Son D-Y, Kim S-G, Seo J-Y, Lee S-H, Shin H, Lee D and Park N-G 2018 Universal approach toward hysteresis-free perovskite solar cell via defect engineering *J. Am. Chem. Soc.* **140** 1358–64

[42] O'Kane S E J *et al* 2017 Measurement and modelling of dark current decay transients in perovskite solar cells *J. Mater. Chem.* C **5** 452–62

[43] Tress W, Marinova N, Moehl T, Zakeeruddin S M, Nazeeruddin M K and Grätzel M 2015 Understanding the rate-dependent J–V hysteresis, slow time component, and aging in $CH_3NH_3PbI_3$ perovskite solar cells: the role of a compensated electric field *Energy Environ. Sci.* **8** 995–1004

[44] Sze S M and Ng K K 2006 *Physics of Semiconductor Devices* (Hoboken, NJ: Wiley) (https://doi.org/10.1002/0470068329)

[45] Kirkpatrick S, Gelatt C D and Vecchi M P 1983 Optimization by simulated annealing *Science* **220** 671–80

[46] van Laarhoven P J and Aarts E H 1987 *Simulated Annealing: Theory and Applications* (Dordrecht: Springer)

[47] Hu Y, Song L, Chen Y and Huang W 2019 Two-terminal perovskites tandem solar cells: recent advances and perspectives *Sol. RRL* **3** 1900080

[48] Chen B, Zheng X, Bai Y, Padture N P and Huang J 2017 Progress in tandem solar cells based on hybrid organic–inorganic perovskites *Adv. Energy Mater.* **7** 1602400

[49] Jiang Y *et al* 2016 Efficient colorful perovskite solar cells using a top polymer electrode simultaneously as spectrally selective antireflection coating *Nano Lett.* **16** 7829–35

[50] Tavakoli M M, Tsui K-H, Zhang Q, He J, Yao Y, Li D and Fan Z 2015 Highly efficient flexible perovskite solar cells with antireflection and self-cleaning nanostructures *ACS Nano* **9** 10287–95

[51] Jošt M, Albrecht S, Kegelmann L, Wolff C M, Lang F, Lipovšek B, Krč J, Korte L, Neher D and Rech B 2017 Efficient light management by textured nanoimprinted layers for perovskite solar cells *ACS Photonics* **4** 1232–9

[52] Paetzold U W, Qiu W, Finger F, Poortmans J and Cheyns D 2015 Nanophotonic front electrodes for perovskite solar cells *Appl. Phys. Lett.* **106** 173101

[53] de Wild J, Meijerink A, Rath J K, Wgjhm V S and Schropp R E I 2011 Upconverter solar cells: materials and applications *Energy Environ. Sci.* **4** 4835–48

[54] Jiang L *et al* 2017 Enhancing the photovoltaic performance of perovskite solar cells with a down-conversion Eu-complex *ACS Appl. Mater. Interfaces* **9** 26958–64

[55] Staub F, Kirchartz T, Bittkau K and Rau U 2017 Manipulating the net radiative recombination rate in lead halide perovskite films by modification of light outcoupling *J. Phys. Chem. Lett.* **8** 5084–90

[56] Staub F, Hempel H, Hebig J-C, Mock J, Paetzold U W, Rau U, Unold T and Kirchartz T, 2016 Beyond bulk lifetimes: insights into lead halide perovskite films from time-resolved photoluminescence *Phys. Rev. Appl.* **6** 044017

[57] Sun X, Asadpour R, Nie W, Mohite A D, and Alam M A 2015 A physics-based analytical model for perovskite solar cells *IEEE J. Photovolt.* **5** 1389–94

[58] Yang G, Wang C, Lei H, Zheng X, Qin P, Xiong L, Zhao X, Yan Y and Fang G 2016 Interface engineering in planar perovskite solar cells: energy level alignment, perovskite morphology control and high performance achievement *J. Mater. Chem.* A **5** 1658–66

[59] Hawash Z, Raga S R, Son D-Y, Ono L K, Park N-G and Qi Y 2017 Interfacial modification of perovskite solar cells using an ultrathin MAI layer leads to enhanced energy level alignment, efficiencies, and reproducibility *J. Phys. Chem. Lett.* **8** 3947–53

[60] Soldera M and Taretto K 2018 Combining thickness reduction and light trapping for potential efficiency improvements in perovskite solar cells *Phys. Status Solidi* a **215** 1700906

[61] Barrows A T, Pearson A J, Kyu Kwak C, Dunbar A D F, Buckley A R and Lidzey D G 2014 Efficient planar heterojunction mixed-halide perovskite solar cells deposited via spray-deposition *Energy Environ. Sci.* **7** 2944–50

[62] Wang S, Sakurai T, Wen W and Qi Y 2018 Energy level alignment at interfaces in metal halide perovskite solar cells *Adv. Mater. Interfaces* **5** 1800260

[63] Staub F, Kirchartz T, Bittkau K and Rau U 2017 Manipulating the net radiative recombination rate in lead halide perovskite films by modification of light outcoupling *J. Phys. Chem. Lett.* **8** 5084–90

[64] Sun X, Asadpour R, Nie W, Mohite A D and Alam M A 2015 A physics-based analytical model for perovskite solar cells *IEEE J. Photovolt.* **5** 1389–94

[65] Staub F, Hempel H, Hebig J-C, Mock J, Paetzold U W, Rau U, Unold T and Kirchartz T 2016 Beyond bulk lifetimes: insights into lead halide perovskite films from time-resolved photoluminescence *Phys. Rev. Appl.* **6** 044017

[66] Nguyen D-T, Vedraine S, Cattin L, Torchio P, Morsli M, Flory F and Bernède J C 2012 Effect of the thickness of the MoO_3 layers on optical properties of MoO_3/Ag/MoO_3 multilayer structures *J. Appl. Phys.* **112** 063505

[67] Motaung D E, Malgas G F, Arendse C J and Mavundla S E 2012 Determination of the structure, morphology and complex refractive index in ZnO-nanopencils/P3HT hybrid structures *Mater. Chem. Phys.* **135** 401–10

[68] Lin Q, Armin A, Nagiri R C R, Burn P L and Meredith P 2015 Electro-optics of perovskite solar cells *Nat. Photonics* **9** 106–12

[69] Pan S S, Zhang Y X, Teng X M, Li G H and Li L 2008 Optical properties of nitrogen-doped SnO2 films: effect of the electronegativity on refractive index and band gap *J. Appl. Phys.* **103** 093103

[70] Datta D, Tripathi V, Gogoi P, Banerjee S and Kumar S 2008 Ellipsometric studies on thin film CuPC: C60 blends for solar cell applications *Thin Solid Films* **516** 7237–40